BNL-224514-2023-JAAM

Proton acceleration in an overdense hydrogen plasma by intense CO2 laser pulses with nonlinear propagation effects in the underdense preplasma

Y. Chen, M. Polyanskiy

To be published in " PHYSICS OF PLASMAS"

May 2023

Accelerator Test Facility

Brookhaven National Laboratory

U.S. Department of Energy

USDOE Office of Science (SC), High Energy Physics (HEP) (SC-25)

DISCLAIMER

Proton acceleration in an overdense hydrogen plasma by intense CO_2 laser pulses with nonlinear propagation effects in the underdense preplasma

Yu-hsin Chen,[1, a)] Antonio C. Ting,[2] Bahman Hafizi,[1] Michael H. Helle,[1] Luke A. Johnson,[3] Mikhail Polyanskiy,[4] Igor Pogorelsky,[4] Marcus Babzien,[4] Nicholas Dover,[5] Oliver Ettlinger,[5] George Hicks,[5] Emma-Jane Ditter,[5] Zulfikar Najmudin,[5] and Daniel F. Gordon[1]
[1)] *Plasma Physics Division, Naval Research Laboratory, Washington, DC 20375, USA*
[2)] *Institute for Research in Electronics and Applied Physics, University of Maryland, College Park, MD 20740, USA*
[3)] *The MITRE Corporation, McLean, VA 22102, USA*
[4)] *Accelerator Test Facility, Brookhaven National Laboratory, Upton, NY 11973, USA*
[5)] *The John Adams Institute for Accelerator Science, Imperial College London, London SW7 2AZ, United Kingdom*

(Dated: 12 December 2022)

We report on proton acceleration from intense CO_2 laser-irradiated hydrogen plasmas at near-critical densities, with the density gradient steepened by Nd:YAG laser ablation-driven hydrodynamic shocks. While the experimental results, including quasi-monoenergetic proton spectra and their scaling law with respect to the laser energy, generally agree with simulations, with some laser shots we observed much higher proton energies than expected. The increased proton energy may be linked to nonlinear propagation effects in the steepened plasma density ramp before the critical surface, including relativistic self-focusing and, for the case of temporally-structured laser pulses observed in the experiment, focusing of the trailing pulse through the plasma channel formed by the leading pulse 25 ps ahead. The occurrence of channel focusing in the underdense hydrogen plasma is supported by a subsequent pump-probe experiment with dark-field imaging technique, where formation of ion channels was observed after the passage of an intense CO_2 laser pulse.

I. INTRODUCTION

Energetic ions can be produced by laser interactions with the plasma at relativistic intensities. Various acceleration mechanisms covering a wide range of laser and plasma parameters have been proposed or identified, such as, to name a few, target normal sheath acceleration (TNSA)[1,2], radiation pressure acceleration (RPA)[3–5], break-out afterburner (BOA) acceleration[6,7], and magnetic vortex acceleration[8,9]. Compared with traditional RF-based ion sources, laser plasma-based ion acceleration is attractive due to its extremely high acceleration gradient ($\sim$ TeV/m). Earlier experimental investigations have mainly focused on overdense plasmas with $n_e \sim 10^2 - 10^3 n_c$ using thin (nm to μm), solid-density targets with high-intensity near-IR lasers at wavelengths of $\sim 1\ \mu$m, where $n_c = m_e\omega^2/(4\pi e^2)$ is the plasma critical density.

Several experiments in relativistic transparency or near-critical density regimes demonstrated energetic ions with relatively narrow energy spreads, which attracted considerable attentions[10–12]. In particular, quasi-monoenergetic protons were produced through intense CO_2 laser interactions with the hydrogen gas target[10,11] at a density close to $n_c \sim 10^{19}$ cm^{-3}. It is generally accepted that acceleration is initiated by the radiation pressure from the laser pulse, or by the thermal pressure from the laser-heated plasma. In Ref. 10, a maximum proton energy of ~ 1 MeV was obtained using a circularly-polarized CO_2 laser pulse with a normalized laser field strength $a_0 \sim 1$. Similar results were produced using the same CO_2 laser system with linear polarization[13,14]. Acceleration is attributed to effects associated with radiation pressure, and ion energy is correlated to hole-boring velocity v_{hb}[15,16], or "piston"-driven electrostatic shocks moving at a velocity v_{sh} on the same order of v_{hb}[17]. In Ref. 11, on the other hand, ~ 20 MeV protons were observed using a linearly-polarized CO_2 pulse train with $a_0 \sim 2.5$ at its peak. Energetic protons appear to be originated from plasma thermal pressure after significant laser heating, leading to an electrostatic shock with the velocity $v_{\mathrm{sh}} \gg v_{\mathrm{hb}}$[11,18].

With CO_2 lasers, access to near-critical density regime becomes straightforward because $n_c \sim 10^{19}$ cm^{-3} at the wavelength $\lambda \sim 10\ \mu$m is comparable with the number density of an ideal gas $\sim 2.7\times10^{19}$ cm^{-3} at standard temperature and pressure conditions. Acceleration of quasi-monoenergetic protons up to 0.6 MeV with a high-density (2.7×10^{21} cm^{-3}) hydrogen gas jet and a high-intensity ($a_0 = 4.2$), 1 μm wavelength laser was also reported[19]. Another recent experiment using high-density H_2 gas jet with $a_0 = 6$ at 1 μm wavelength produced 6 MeV protons with small energy spreads[20]. The gas target is simple, low-cost, replenishable, and debris-free compared with solid targets, which makes it exceptionally suitable for high-repetition-rate accelerator applications.

In contrast to solid-density objects, a volume of gas

[a)] Electronic mail: yu-hsin.chen@nrl.navy.mil

usually does not have a well-defined mass-vacuum boundary. For gas targets used in aforementioned proton acceleration experiments with CO_2 lasers[10,11,13,14], a density ramp up to n_c with a length scale of ~ 1 mm is present. Such a thick underdense layer can parasitically absorb laser energy[13,21], and various approaches of density profile shaping have been employed to significantly steepen the density ramp at the front side of the gas target in those experiments[11,13,14]. On the other hand, it is found that under some circumstances, the underdense plasma layer can be beneficial to ion acceleration. In TNSA, an adequate thickness of underdense preplasma may increase accelerated ion energies due to self-focusing of the laser pulse[22,23] and efficient heating of electrons[24,25]. For ultrathin (< 1 μm) solid targets, it is suggested that self-focusing in the relativistic transparent plasma may contribute to enhanced ion acceleration[26].

Here we report on proton acceleration experiment using moderately relativistic ($a_0 \sim 1$) CO_2 laser pulses in the near-critical ($\sim 2n_c$) hydrogen gas target, with the density profile tailored by ablation-driven hydrodynamic shocks. Application of such density shaping technique in CO_2 laser-driven ion acceleration experiment was briefly mentioned in Ref. 14. While the experimental results, including quasi-monoenergetic proton spectra and their scaling law with respect to the laser energy, are in reasonable agreement with simulations, with some laser shots we observed much higher proton energies than expected. This is possibly caused by relativistic self-focusing of the laser pulse in the sub-critical density ramp. Furthermore, it is found that a post-pulse with a fraction (typically $\sim 50\%$) of the main pulse energy could also play an important role in accelerating protons. Calculations show that the transverse ponderomotive force of the main pulse may produce an ion channel in the underdense plasma[27,28], which results in strong focusing with significant intensity increase of the post-pulse 25 ps after the main pulse. Spatially-resolved proton energy spectra indicated that acceleration might be affected by these nonlinear propagation effects. The laser-produced ion plasma channel was directly observed in a subsequent experiment, where a weak, collinear probe pulse was coupled into a guiding structure 40 ps after the intense CO_2 laser pulse.

II. EXPERIMENTAL SETUP AND STEEPENING OF GAS DENSITY PROFILE

The experiment was conducted using a terawatt, picosecond CO_2 laser at Accelerator Test Facility (ATF), Brookhaven National Laboratory. The laser pulse is focused to a vacuum spot size of $w_0 \sim 60$ μm near the center of a hydrogen gas target by an f/3 off-axis parabolic mirror (OAP). The interaction region is transversely probed by fundamental and frequency-doubled, mode-locked Nd:YAG laser pulses with ~ 10 ps duration and variable delays, for interferometry and shadowgraphy. Protons are detected by an ion spectrometer aligned to the laser propagation axis after the interaction region.

The ATF laser consists of a short-pulse solid-state seed laser with two high-pressure CO_2 amplifiers. At the time of the experiment, the amplification stages are configured as chirped-pulse amplification (CPA) in the preamplifier[29], followed by direct short-pulse amplification in the main amplifier. Gain narrowing and limited spectral line broadening with 8 atm $^{12}C^{16}O_2$ gas mixture in the main amplifier result in a main pulse with a duration of ~ 3.5 ps, followed by ~ 2 lower-energy post-pulses temporally spaced by 25 ps, and the maximum total laser energy in the experiment is approximately 5 J. During the experiment, the laser temporal profile is recorded for each shot by a streak camera with ~ 1 ps resolution, after nonlinear frequency shifting a small portion of laser energy to ~ 1 μm wavelength[29]. A typical temporal waveform is shown as the inset of Fig. 1. Such temporal structure is crucial in explaining our experimental results, which will be discussed later.

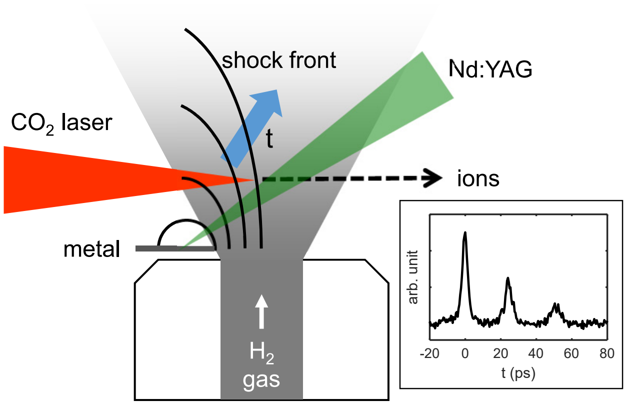

FIG. 1. Experimental setup. Inset: a typical measured temporal structure of the CO_2 laser, showing two post-pulses after the main pulse with an interpulse spacing of 25 ps.

The hydrogen target is produced by a gas jet nozzle with ~ 1 mm orifice diameter. Within the operating range of the backing pressure, the peak gas density in the jet is 10^{18}–10^{19} cm^{-3} with ~ 1 mm-long density up-ramp along the laser propagation axis. To create a density profile suitable for proton acceleration, the gas volume is compressed and steepened from the edge with hydrodynamic shocks, created by laser ablation of a solid-density material in the vicinity. The technique was demonstrated at Naval Research Laboratory[30,31], and was later used to produce a high-density (up to 5×10^{20} cm^{-3}), sub-100-μm-thick "gas foil" for proton acceleration via laser-driven pinch current followed by Coulomb explosion in the plasma[32]. Here we focus a 70 mJ, 1064 nm nanosecond Nd:YAG laser pulse with f/20 onto a piece of stainless steel sheet, mounted at the edge of the nozzle orifice without severely disturbing the gas flow, as shown in Fig. 1. A spherical blast wave is launched from the point of ablation into the gas column. By choosing an appropriate delay ~ 30 ns between Nd:YAG and CO_2 pulses, as well as a suitable CO_2 beam height, the CO_2 pulse propagates through the cavitation region until encountering a sharp density jump near the shock front, at a nearly normal angle of incidence. At this moment, the shape of the shock front becomes ellipsoidal due to spatial variation of gas density that causes anisotropic shock expansion.

Figure 2(a) shows a representative interferogram of the interaction region when quasi-monoenergetic protons are produced, recorded ~ 30 ps after CO_2 pulse interaction with the shock-compressed gas jet. The plasma-induced, abrupt negative phase shift within $\sim 100\ \mu$m across the hydrodynamic shock front is clearly visible. Note that the laser spot radius is about $60\ \mu$m while almost the whole shocked region (> 2 mm in height in Fig. 2(a)) is ionized. Ionization far beyond the region of interest, which is caused by fast electrons emitted near the focus[13], creates difficulties in extracting the density profile with Abel inversion because the assumption of cylindrical symmetry is no longer valid in our case. To estimate the density profile, especially the length scale of the density up-ramp at the laser entrance side, we employ self-similar solutions of the strong spherical shock from a point source of explosion[33,34]. This is to evaluate $n_{\mathrm{H}_2}(|\mathbf{r}|/R) = n_{\mathrm{H}_2,\mathrm{hs}}\eta_s(|\mathbf{r}|/R)$ along the laser propagation axis, where $|\mathbf{r}| = [(y-y_0)^2 + (z-z_0)^2]^{1/2}$ is the distance from the source of explosion (y_0, z_0) to a point (y, z) on the laser axis, R is the distance between the source and the shock front along the direction $\hat{\mathbf{r}}$, $n_{\mathrm{H}_2,\mathrm{hs}}$ is the gas density estimated at the hydrodynamic shock front with planar approximation, and $\eta_s(|\mathbf{r}|/R)$ is the self-similar solution of the density normalized to unity at the shock front. Note that for strong explosion in a uniform gas, the self similar solution gives the temporal evolution $R(t) = \xi_0(E_{\mathrm{abs}}/\rho_0)^{1/5}t^{2/5}$ with $\xi_0 = 1.033$ for ideal diatomic gases, where E_{abs} is the explosion energy absorbed by the gas, and ρ_0 is the mass density[33,34]. From Fig. 2(a) it is found that gas density at the shock front generally agrees with $R \propto (1/n_{\mathrm{H}_2,\mathrm{hs}})^{1/5}$ as well. The plasma density profiles along laser propagation axis, with and without shock compression and steepening, are shown in Fig. 2(b). Peak density at the shock front is increased by a factor of 4 to $\sim 2 \times 10^{19}$ cm^{-3}, which is close to the theoretical limit of $(\gamma_{\mathrm{H}_2} + 1)/(\gamma_{\mathrm{H}_2} - 1) = 6$ in the strong shock regime, where $\gamma_{\mathrm{H}_2} = 7/5$ is the specific heat ratio of hydrogen. The density gradient averaged between $10\% - 100\%$ peak density is increased from $\sim 0.6 \times 10^{19}$ cm^{-3}/mm to $\sim 9 \times 10^{19}$ cm^{-3}/mm by a factor of 15.

We remark that ionization outside the main region of laser-plasma interactions can be also contributed by the low-intensity periphery of the focal spot. While the tunneling ionization threshold intensity of hydrogen is around 10^{14} W/cm^2, the avalanche breakdown threshold intensity near the shock front may be significantly lower, which is estimated by[35] I_{th} [TW/cm^2] $\sim 470U_{\mathrm{eV}}/(n_{19}\tau_{\mathrm{ps}}\lambda_{\mu\mathrm{m}}^2) \sim 10$. Here $U_{\mathrm{eV}} = 15.4$ and $n_{19} \sim 1$ are the ionization energy in eV and the number density in 10^{19} cm^{-3}, respectively, for H_2 molecules, while τ_{ps} is the laser FWHM pulse duration in ps and $\lambda_{\mu\mathrm{m}}$ is the laser wavelength in μm. Prior to arrival of the CO_2 laser pulse, some gas molecules can be pre-ionized in the vicinity of YAG laser ablation site and expand with the shock, which provide seed electrons for the avalanche process. Low-density electrons ($\sim 10^{15} - 10^{16}$ cm^{-3}) were observed within the "void" between the ablation site and the shock front by interferometry, while the CO_2 laser was off. By assuming a uniform illumination of I_{th} in a 1-mm-radius "halo" that ionizes the shock-compressed region as shown in Fig. 2(a), the Strehl ratio (ratio of laser energy within the focal spot to total delivered energy) is approximately 75%, which is reasonable for a high-power, short-pulse laser system.

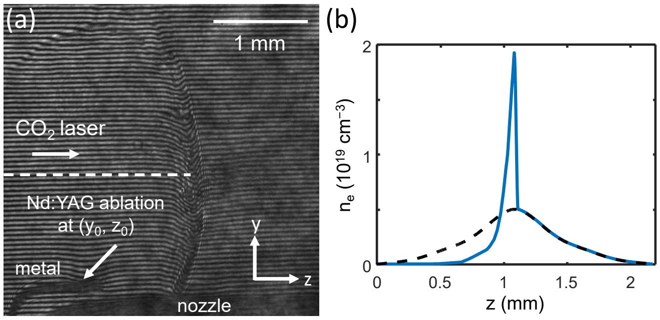

FIG. 2. (a) Interferogram of the hydrodynamic shock-tailored hydrogen target, probed by a 10 ps, frequency-doubled Nd:YAG laser pulse ~ 30 ps (check) after interaction with the CO_2 laser, and (b) estimated plasma density profile along the laser propagation path, with (blue solid curve) and without (black dashed curve) steepening by the YAG-driven hydrodynamic shock.

III. PROTON ACCELERATION: EXPERIMENTAL RESULTS AND SIMULATIONS

The ion spectra are measured by a Thomson parabola[36] (TP) with its entrance pinhole (0.6 mm diameter) located approximately 15 cm after the interaction region at 0° angle with respect to laser axis. The particle detector is a BC-408 plastic scintillator, and its fluorescence is imaged by an electron-multiplying charge-coupled device (EMCCD) camera. The scintillator is covered by a ~ 2-μm-thick aluminum foil, which cuts off stray photons as well as protons with energies lower than ~ 0.2 MeV according to SRIM code[37]. The energy-dependent proton-to-photon yield of the scintillator was calibrated in a previous measurement[38]. During the experiment, energetic proton peaks in the range of $0.4 - 2.6$ MeV with narrow spreads were routinely produced at various laser energies. Figures 3(a) and 3(b) show two typical proton spectra consisting of a high-energy peak ($E_p = 0.8$ MeV for Fig. 3(a) and $E_p = 2$ MeV for Fig. 3(b), respectively) and a low-energy tail. The inset of Fig. 3(a) also shows the scintillator fluorescence image as the raw data from TP. Spectra with multiple peaks were also observed such as the example shown in Fig. 3(c) (0.9 MeV and 1.4 MeV), which will be discussed later. The energy spread of the peak $\Delta E_p/E_p$ in general is less than $\sim 10\%$, after correcting for the finite acceptance angle of TP. Despite of the common features, the spectra shown in Figs. 3(a)–(c) are quite different while the laser energies are similar.

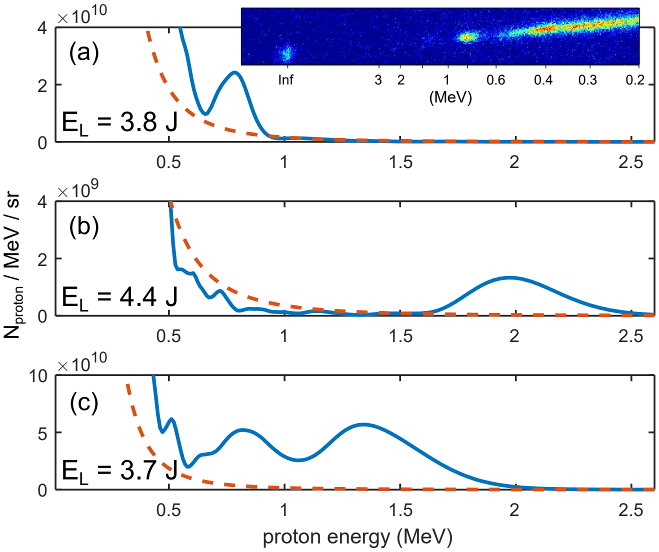

FIG. 3. Representative proton spectra recorded in the experiment, showing (a) a spectral peak at 0.8 MeV (laser energy $E_L = 3.8$ J), (b) a spectral peak at 2 MeV ($E_L = 4.4$ J), and (c) double peaks at 0.9 and 1.4 MeV ($E_L = 3.7$ J). The red dashed curves are the lower detection limit. Vertical axes are scaled to show the quasi-monoenergetic peaks, which are not deconvolved with the entrance pinhole diameter of the Thomson parabola. For spectrum in (a), the raw data from the Thomson parabola is shown in the inset.

Streak camera measurement of laser temporal profile indicates that the energy ratio between each pulse in the pulse train varies shot to shot significantly during the experiment. With the assumption that main interactions are contributed by the first, most intense pulse, Figure 4 shows the energy of the quasi-monoenergetic proton spectral peak versus the first CO_2 laser pulse energy in the pulse train. For the shots with multi-peaked spectra, the proton peak with highest energy is selected. In the regime of near-critical plasmas, hole-boring acceleration (HBA) and shock wave acceleration (SWA) are the candidate processes for production of mono-energetic ions. For HBA, radiation pressure pushes the front surface of the target forward at the hole-boring velocity $v_{\rm hb}/c = [n_c Z m_e/(2 n_e m_i)]^{1/2} a_0$, where Z is the atomic number and m_i is the ion mass[15]. Ions are reflected off by the charge separation field near the moving mass-vacuum boundary and acquire a velocity $v_{i,\rm hb} = 2 v_{\rm hb}$. In SWA, a collisionless electrostatic shock is launched into the plasma when $v_{\rm hb}$ created by the incident laser is greater than the local ion sound speed, which is usually satisfied for an initially cold, near-critical plasma in the relativistic laser field with the condition[17] $a_0 \gtrsim 2\alpha(n_e/n_c)$ where $\alpha \sim 1/3 - 1/2$. For $v_{\rm hb} \ll c$ the velocity of the electrostatic shock can be estimated by $v_s/c = [n_c Z m_e/(2 n_e m_i)]^{1/2} a_0 (1+\gamma_p)/2 = 1.3 v_{\rm hb}/c$ where $\gamma_p = 5/3$ is the adiabatic index for an ideal gas[17], and ions can be accelerated to $v_{i,s} = 2 v_s$ at the shock front. Estimated proton energies from both HBA and SWA models are shown in Fig. 4 by letting $n_e = n_c$, with the assumption that the main interaction occurs at the critical surface.

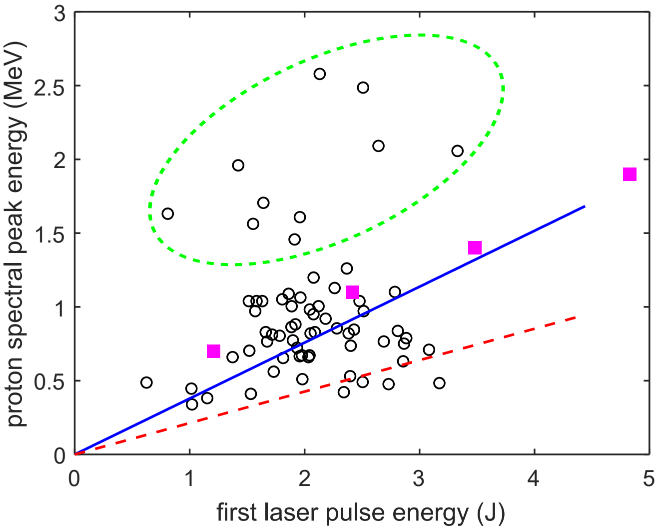

FIG. 4. Highest proton spectral peak energy from each shot with respect to the main (first) laser pulse energy in the pulse train (black open circles), compared with HBA (red dashed line) and SWA (blue solid line) models, as well as 1-D PIC simulations (magenta filled square). The “outliers” with much higher proton energies than predictions from models and simulations are marked by the green dashed oval.

In the attempt to further understand our experimental results, we performed a series of 1-D (1D3V) particle-in-cell (PIC) simulations using turboWAVE code[39–41] at a laser pulse duration of 3.5 ps, with a range of peak intensities $a_0 = 0.7 - 1.4$ corresponding to $1.2 - 4.8$ J pulse energies. To address the most relevant physics, we used a fully-ionized, cold hydrogen plasma with a density profile shown in the inset of Fig. 5(d), which has a similar peak density but a shorter up-ramp than that of the hydrodynamic shock-tailored profile in Fig. 2(b). A downscaled 3-D PIC simulation with 100 fs pulse duration and $a_0 = 1$ was first carried out. Self-focusing of the pulse in the underdense up-ramp is negligible, which motivates the use of 1-D simulations here. For laser propagation in the hydrodynamic shock-tailored profile shown in Fig. 2(b), transverse nonlinear effects could be significant, which will be discussed later. The 1-D simulation box is 430 μm in length and the cell size is 52.6 nm. The number of particles for each species is scaled with the density profile, and 243 particles in one cell corresponds to a density of 10^{19} cm^{-3}. Simulations show that the most energetic

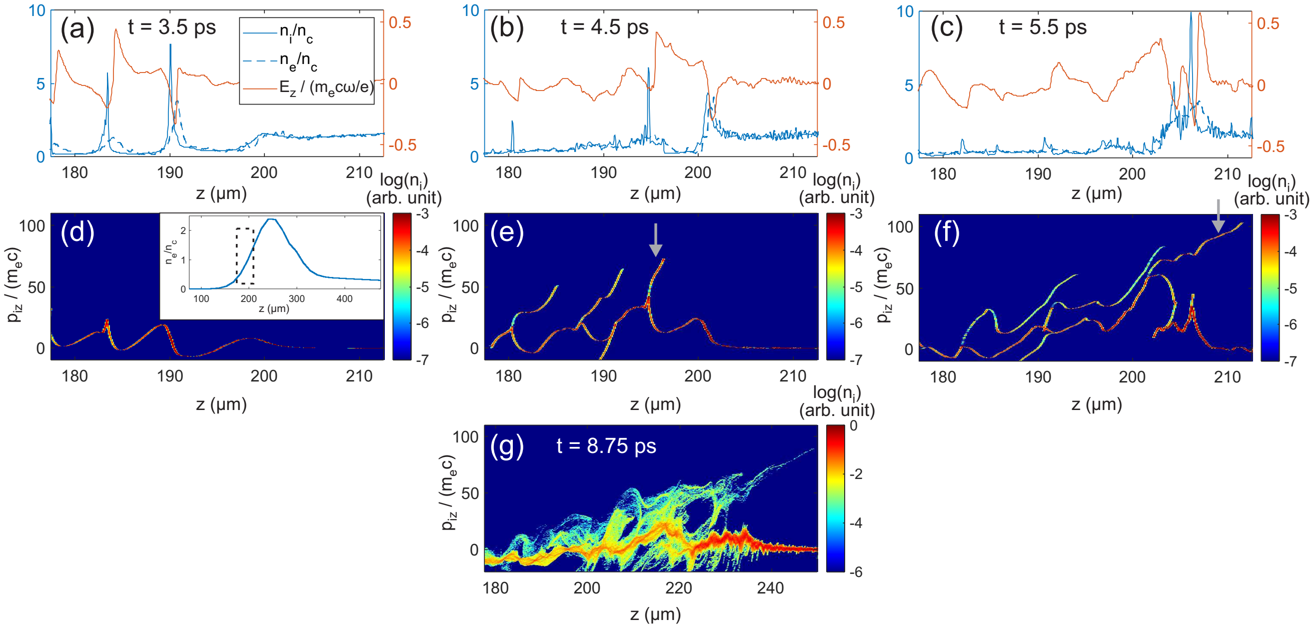

FIG. 5. Results of 1-D PIC simulation showing the process of proton acceleration at (a)(d) $t = 3.5$ ps, (b)(e) $t = 4.5$ ps, and (c)(f) $t = 5.5$ ps after the 3.5 ps, $a_0 = 1$ laser pulse is launched from the left boundary of the simulation box at $z = 75$ μm. The inset of (d) is the initial density profile of the hydrogen plasma, and simulation results within the region marked by the dashed rectangle are shown here. The critical surface is located at $z \sim 200$ μm before simulation starts. The same proton bunch marked by the arrow in phase space diagrams (e) and (f) encounters two acceleration structures with positive E_z shown in (b) ($z \sim 195 - 200$ μm) and (c) ($z \sim 207 - 208$ μm) while moving in $+z$ direction. Energy of the proton bunch is about (e) 0.6 MeV at $t = 4.5$ ps and reaches $\sim$ 0.9 MeV at $t = 5$ ps (not shown), and is further accelerated to (f) $\sim$ 1.1 MeV at $t = 5.5$ ps. (g) The phase space diagram (z, p_{iz}) from a 2-D PIC simulation with $a_0 = 1$, averaged over $-4.2 \leq x \leq 4.2$ μm, shows $\sim$ 1 MeV accelerated protons at $t = 8.75$ ps.

protons originate from a two-stage acceleration process, and the result for $a_0 = 1$ is shown in Fig. 5. First, the incident laser pulse and its reflection from the critical surface create a standing wave, which forms density ripples of electrons and ions with the scale of a laser wavelength in the underdense region[42]. In the mean time the laser pulse also pushes the critical surface forward and steepens its density gradient. The ion density modulation grows to form sharp spikes with densities of several n_c and thicknesses of sub-μm (Figs. 5(a) and 5(d)). Protons are accelerated from these structures while an electrostatic shock front is about to form at the critical surface (Figs. 5(b) and 5(e)). The proton bunch from the nearest ion density spike then catches up the shock front leaving the critical surface, and is further accelerated to a center energy of $\sim$ 1.1 MeV with a relatively narrow energy spread (Figs. 5(c) and 5(f)). Simulated proton center energies with $a_0 = 0.7, 1, 1.2, 1.4$ are shown in Fig. 4. Finally, a 2-D PIC simulation with $a_0 = 1$ at a lower resolution (box size 345 (x) $\times$ 862 (z) μm^2, cell size 168 (x) $\times$ 105 (z) nm^2, with 135 particles in a cell corresponding to $n = 10^{19}$ cm^{-3} for each species) is carried out. The general features of particle and field evolution qualitatively agree with the 1-D simulation. Protons are accelerated to $\sim$ 1 MeV according to the axial phase space diagram shown in Fig. 5(g), which is similar to the 1-D result in Fig. 5(f). While predictions with HBA and SWA models as well as 1-D PIC simulations generally agree with most of the experimental results shown in Fig. 4, there are a few "outliers" (marked in Fig. 4) with much higher energies up to 2.5 MeV that cannot be explained. Such discrepancy motivates further investigations into other possibilities related to nonlinear propagation effects which may increase the laser intensity before onset of ion acceleration.

IV. SELF-FOCUSING AND FOCUSING BY A PREFORMED ION CHANNEL IN THE PLASMA

A. Source-dependent expansion (SDE) analysis for nonlinear propagation in the non-uniform plasma

Nonlinear propagation and guiding of a short laser pulse in the plasma, with or without a preformed structure, has been extensively studied[28]. Here we take the approach of analyzing laser spot size evolution in the plasma in the quasi-static limit, following the formalism in Ref. 43 outlined below. Plasma is assumed fully ionized with immobile ions, and laser-plasma instabilities are ignored. For linearly polarized laser field, the paraxial wave equation for the vector potential is solved under cylindrical symmetry using the technique of source-dependent expansion (SDE)[44,45], with the refractive index in the form of[43]

$$\eta^2(r,z) = \frac{\omega^2}{c^2k^2} + \frac{i}{k^2}\frac{\partial k}{\partial z} - \frac{k_p^2}{k^2\sqrt{1+\frac{a^2}{2}}} \times \left(1 + \frac{\nabla_\perp^2\sqrt{1+\frac{a^2}{2}}}{k_p^2} + \frac{r^2}{R_{\mathrm{ch}}^2}\right), \tag{1}$$

where $k_p = (4\pi e^2 n_{e0}(z)/m_e c^2)^{1/2}$ is the plasma wave number of on-axis electron density profile $n_{e0}(z)$, $a = \sqrt{2e^2\lambda^2 I/(\pi m_e^2 c^5)}$ is the slowly varying amplitude of normalized vector potential, and I is the laser intensity envelope (in cgs unit here). The last term on the right hand side of Eq. 1 contains relativistic self-focusing (with relativistic electron mass factor $\sqrt{1+a^2/2}$) and ponderomotive focusing (with a factor $\nabla_\perp^2\sqrt{1+a^2/2}$ representing equilibrium between radial density perturbation and laser ponderomotive force[28]), and can also include a preformed plasma channel with a radius

$$R_{\mathrm{ch}}(z) = \sqrt{\frac{2n_{e0}(z)}{d^2 n_e(r,z)/dr^2}} \tag{2}$$

assuming a parabolic radial density profile with an axial variation $n_e(r,z)$. The preformed plasma channel can serve as an "indestructible" waveguide for applications such as laser wakefield acceleration[46]. In addition, it has also been proposed to use the preformed plasma channel to focus, or more generally, manipulate the spot size and the divergence of an intense laser pulse[47]. The laser beam radius evolution can be obtained by solving[43]

$$\frac{d^2X}{dz^2} + \left(\frac{\omega}{cka_0^2/2}\frac{1}{Z_R}\right)^2\frac{\partial V}{\partial X} = 0 \tag{3}$$

with a normalized spot size $X = \sqrt{2}r_s/(a_0 w_0)$, where r_s is $1/e^2$ beam radius, a_0 and w_0 are maximum normalized field amplitude and minimum spot (waist) radius, respectively, in vacuum, and $Z_R = \omega w_0^2/(2c)$ is the Rayleigh range. $\partial V/\partial X$ is given by[48]

$$\begin{aligned}\frac{\partial V}{\partial X} = &-16\frac{P}{P_c}X\left[1-\sqrt{1+\frac{1}{X^2}}-2\ln 2\right.\\ &\left.+2\ln\left(1+\sqrt{1+\frac{1}{X^2}}\right)\right]-\frac{\ln\left(1+\frac{1}{X^2}\right)}{X}\\ &-2NX\left\{2X^2\left[1-\sqrt{1+\frac{1}{X^2}}-\ln 2\right.\right.\\ &\left.\left.+\ln\left(1+\sqrt{1+\frac{1}{X^2}}\right)\right]{}_4F_3\left(\tfrac{1}{2},1,1,1;2,2,2;\tfrac{-1}{X^2}\right)\right\},\end{aligned} \tag{4}$$

where P is the laser power, $P_c = (k_p a_0 w_0/4)^2/2$ is the critical power for relativistic self-focusing, $N = [8(P/P_c)/(k_p R_{\mathrm{ch}})]^2$ represents the combined focusing strength from relativistic and ponderomotive focusing, and ${}_pF_q$ is the generalized hypergeometric function of order q and class $q-p+1$.

B. Formation of a plasma channel with laser-driven ion motions

For an intense, short (fs – ps) laser pulse in the plasma, ponderomotive force expels electrons radially out from the laser axis, leading to a space charge which exerts an electrostatic force on ions. While the motion of massive ions is usually negligible within the duration of the laser pulse, ion radial drift can continue after the laser pulse is vanished and forms a hollow channel along the trail of the laser pulse. Guiding through a preformed, ponderomotively produced plasma channel in the regime of femtosecond pulse duration was experimentally demonstrated[27,49]. Formation of channel structure is also observed in the picosecond laser-plasma experiment[50,51]. To calculate the evolution of the channel profile, we employ the Green's function method for the the wave equation of normalized ion density modulation $\delta n_i/n_{i0}$[27,28]

$$\left(\frac{\partial^2}{\partial t^2} - C_s^2\nabla_\perp^2\right)\frac{\delta n_i}{n_{i0}} = \frac{Zm_e}{m_i}\nabla_\perp^2\sqrt{1+\frac{a^2}{2}} \tag{5}$$

obtained from continuity and momentum equations of ions, as well as balancing the radial force of electrons. After a change of variables $\zeta = z - ct$ with the assumption that laser group velocity v_g is close to c, the solution to Eq. 5 is[27,28]

$$\begin{aligned}\frac{\delta n_i(\zeta,\mathbf{r})}{n_{i0}} = &\frac{Zm_e c}{2\pi m_i C_s}\int_{-\infty}^{\infty}d\zeta'\int_{-\infty}^{\infty}dx'\int_{-\infty}^{\infty}dy'\\ &\times\frac{\Theta\left(C_s\left(\zeta-\zeta'\right)/c-|\mathbf{r}-\mathbf{r}'|\right)\nabla_\perp'^2\sqrt{1+\frac{a^2}{2}}}{\left[C_s^2\left(\zeta-\zeta'\right)^2/c^2-|\mathbf{r}-\mathbf{r}'|^2\right]^{1/2}},\end{aligned} \tag{6}$$

where $C_s = (Zk_BT_e/m_i)^{1/2}$ is the ion sound speed assuming $T_i \ll T_e$, and $\Theta\left(C_s\left(\zeta-\zeta'\right)/c-|\mathbf{r}-\mathbf{r}'|\right)$ is the Heaviside step function that forces the integrand to be zero for $|\mathbf{r}-\mathbf{r}'|/C_s > (\zeta-\zeta')/c$. Here we have omitted the axial component of the ponderomotive force, which is justified by our laser spot size ($w_0 = 60$ μm) being much smaller than the pulse length ($c\tau_L = 1$ mm). Also note that for the radial component of ponderomotive force, the exact form $\sim \nabla_\perp\sqrt{1+a^2/2}$ is used, in contrast to Refs. 27 and 28. This is important owing to the high intensities in the experiments here, where $a \ll 1$ does not hold.

For convenience we assume a pulse profile $a^2(r,\zeta) = a_0^2\exp\left(-2r^2/w_0^2\right)\sin^2\left(\pi\zeta/(2c\tau_L)\right)$, and compute Eq. 6 numerically for hydrogen plasma. An unknown parameter is the electron temperature T_e, which is not straightforward to determine. Therefore we first examine the dependence of ion channel formation on T_e by choosing a peak intensity $a_0 = 0.5$ and a range of T_e values between 0.05 – 50 keV. The evolution of on-axis density depression is shown in Fig. 6(a), while the radial profile of the channel at the delay of $\zeta/c = 25$ ps (interpulse separation of the $\mathrm{CO_2}$ laser pulse train in our experiment) is shown in Fig. 6(b). At lower electron temperature, change of axial ion density after the passage of the laser pulse approaches linear with respect to the delay. This is because the electron pressure becomes negligible and does not slow down the drift motion of ions. Within the delay of our interest, the channel density profile is not sensitive to the electron temperature for $T_e < 2$ keV. Therefore precise knowledge to T_e is not required, while previous measurements indicate that the temperature of intense laser-ionized, underdense plasma is generally in the range of $\sim 0.1 - 1$ keV[27]. With $T_e = 0.2$ keV, calculated axial density perturbation $\delta n_i(r = 0, \zeta)/n_{i0}$ as well as the radial profile $\delta n_i(r, \zeta = c \times 25 \text{ ps})/n_{i0}$ are shown in Figs. 7(a) and 7(b), respectively, at various laser intensities. For $a_0 \gtrsim 0.8$, an unphysical result of $\delta n_i/n_{i0} < -1$ at $\zeta/c = 25$ ps is obtained. Although Eq. 6 does not work at the highest intensities matching our experimental conditions ($a_0 \sim 1$), it is still instructive to study the channel formation at lower intensities. By substituting n_{e0} with $n_{i0} + \delta n_i$ in Eq. 2 and fitting Fig. 7(b) with parabolic curves, the plasma channel width R_{ch} versus a_0 25 ps after the laser pulse is extracted and shown in Fig. 7(c).

C. SDE calculation results for laser propagation in a plasma density ramp with and without a preformed channel

Equation 3 is then solved numerically, using a fitted axial density profile up to n_c shown in Fig. 8(a) from the ablation-tailored plasma density ramp in Fig. 2(b), without a preformed radial structure ($R_{\text{ch}} \to \infty$). The change in beam radius along laser axis for the cases of (vacuum focus) $a_0 = 0.001$ (representing linear propagation), 0.5, 0.7, and 1 are presented in Fig. 8(a). The vacuum focus is placed at the location with $n_e \sim 0.1 n_c$, and for $a_0 \geq 0.5$ significant focusing effect can be observed while propagating along the density ramp. As a check of the SDE analysis, we ran a simulation with $a_0 = 1$ using ponderomotive guiding center (PGC)[39,40] module of turboWAVE code. The PGC algorithm is an approximation to full 3D PIC code, by simulating the slow-varying envelope of the laser field instead of resolving each optical cycle. To further speed up the simulation we used radially symmetric geometry with a laser pulse duration of 1 ps. An effective beam radius $r(z) = r(z_0)(I_{\text{peak}}(z)/I_{\text{peak}}(z_0))^{1/2}$ is obtained from the simulated peak intensities I_{peak}, where z_0 is the laser pulse location in the beginning of the simulation. Although PGC algorithm, which is valid for $\omega \gg \omega_p$, begins to break down when the plasma density reaches $\sim 0.2\ n_c$, the beam size evolution shows that deviation from linear propagation starts at lower density ($\sim 0.03 n_c$) region, which indicates self-focusing and qualitatively agrees with the SDE results.

To reveal the possible effect of the plasma channel, created by the first CO_2 laser pulse in the pulse train, on the propagation of the second pulse, we use $R_{\text{ch}} = 33\ \mu$m and $\delta n_i/n_{i0} = -0.5$ from Fig. 7 (produced by the first pulse with $a_0 = 0.5$) and solve Eq. 3. We do not consider any R_{ch} and $\delta n_i/n_{i0}$ values obtained from $a_0 > 0.5$, so that the requirement $|\delta n_i/n_{i0}| \ll 1$ for Eq. 6 is generally satisfied. In this case, the effect of channel focusing on the second pulse is significant as shown in Fig. 8(b): while the first pulse ($a_0 = 0.5$) undergoes slight self-focusing with the spot radius reduced to $\sim 55\ \mu$m ($\sim 10\%$ smaller than its vacuum spot) near the critical surface, a low-intensity ($a_0 = 0.001$) trailing pulse 25 ps after the passage of the first pulse can be focused to $\sim 10\ \mu$m radius in the plasma density ramp. When increasing the intensity of the second pulse to $a_0 = 0.5$, it can be seen that channel focusing is still the dominant effect. The spot size evolution is nearly unchanged compared with the low energy case, until the laser pulse reaches higher density region at $z \sim 1$ mm.

D. Nonlinear laser propagation inferred by observed proton spectra in the experiment

While the above analysis is conducted at a lower laser intensity than that in our experiment without considering other effects such as instabilities, it may still provide some insights on explaining our experimental results. The "outlier" shots marked in Fig. 4 with much higher-than-expected proton energies are now examined more closely, and it is found that the proton spectrum is correlated with the laser pulse temporal profile: two of these shots produced single quasi-monoenergetic proton spectral peaks, while the rest generated structured spectra with two or more peaks at the high energy end. These two particular shots actually came with one single laser pulse (or at least the post pulses are below the detection level), and the rest had one or more apparent post pulses in addition to the main one, as the examples shown in Fig. 9. One may therefore assert that the first post pulse (subsequent post pulses are ignored due to their lower energy) must have contributed to at least one of the two highest-energy proton spectral peaks. Again the intensities of post pulses, estimated from vacuum spot size, are not sufficient to produce protons with these energies as shown in Fig. 9(e), according to the simulations and the acceleration models discussed earlier. These observations imply that relativistic self-focusing of the main laser pulse, as well as, for the case that the post pulse is present, formation of an ion channel by the main pulse followed by channel focusing of the post pulse, are both likely the origins of elevated proton energies owing to increased laser intensities in the plasma density ramp before the critical surface.

Although our experimental apparatus did not have a diagnostic for direct observation of the plasma channel, some indirect evidence on its existence was noted from the experimental results. During the experiment we replaced the entrance pinhole of TP with a 500-μm-wide slit, and turned off the high-voltage bias to observe the proton beam profile. While X-ray emission (signal at "infinite proton energy" in Fig. 10) from the interaction

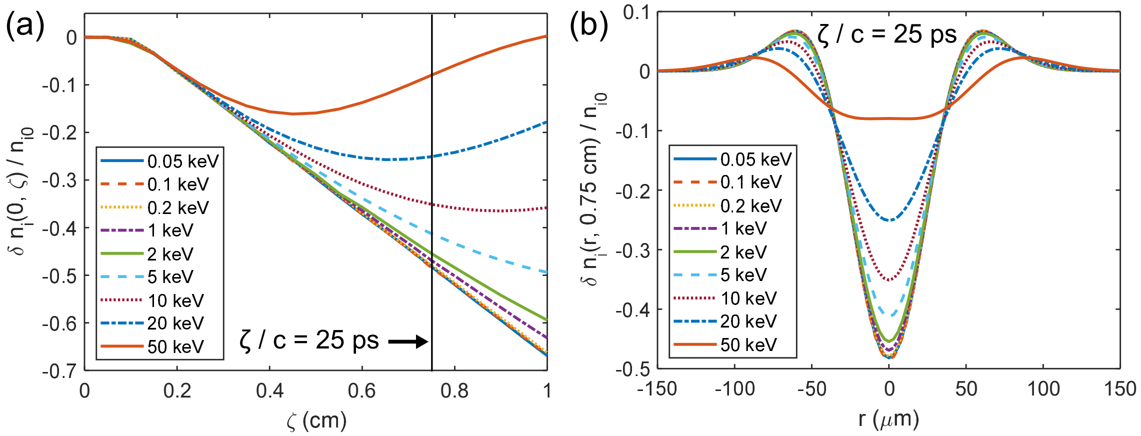

FIG. 6. Calculated (a) temporal evolution of on-axis ion density perturbations up to $\zeta/c = 33$ ps, and (b) radial ion channel profiles at $\zeta/c = 25$ ps, with a range of electron temperature $T_e = 0.05 - 50$ keV in a hydrogen plasma. The laser intensity is $a_0 = 0.5$ with a pulse duration of 3.5 ps.

region is angularly uniform within the length of the slit, proton beams in general contain spatial-spectral structures with substantial shot-to-shot variations as demonstrated by example spectra in Fig. 10. The high-energy, narrow-spread spectral components of the proton beam often exhibit much reduced divergence and erratic pointing angles. The pointing fluctuation suggests that the laser pulse may have undergone hosing[51–55] and produced a modulated density channel in the underdense plasma, which was previously observed in the simulation and the experiment. The collimated beam profile, such as the one with a narrow divergence angle of ∼ 8 mrad at ∼ 2 MeV in Fig. 10(b), may be also associated with the channel formation but further studies are required to understand its origin. (Collimated energetic protons were observed in laser interactions with underdense plasmas[19].) In Figs. 10(a), (c) and (d), the collimated MeV proton beams are partially blocked at the ends of the entrance slit, so that their divergence angles cannot be determined. On the contrary, the low-energy component ($\lesssim 0.5$ MeV) of the proton beam is spectrally and spatially more uniform. The thermal-like spectrum (which is better revealed after correcting for the instrument response) implies that these low energy protons may be produced by TNSA at the back side of the overcritical region, which is relatively insensitive to laser beam pointing.

V. EXPERIMENTAL OBSERVATION OF HOLLOW PLASMA CHANNELS PRODUCED BY INTENSE CO$_2$ LASER PULSES

In order to gather evidence of possible plasma channel formation that may lead to high-energy protons through channel focusing of the post pulses, we performed a subsequent channel observing experiment. Prior to the experiment, the ATF CO$_2$ laser had undergone a major upgrade[56]. The laser pulse duration is reduced to ∼ 2 ps, and the post pulses are nearly eliminated. The beam quality is also improved, with a vacuum focal spot $1/e^2$ radius of ∼ 35 μm. For this experiment we used an underdense hydrogen plasma with ∼ 1 mm length from a pulsed gas jet similar to the one used in the proton acceleration experiment. A low-energy, 532 nm, 10 ps probe with variable delay co-propagates with the CO$_2$ pump laser pulse through the plasma with $n_e \sim 3\times10^{18}$ cm^{-3} in the configuration of dark-field imaging (Fig. 11). While the pump pulse is focused by the f/3 OAP into the plasma, the collimated probe pulse passes through a 5-mm-diameter hole on OAP to combine with the pump and overfills its focal spot. A rectangular-shaped pickoff mirror is placed slightly off-axis at ∼ 10 cm after the pump focus, so that the collimated probe (and also ions) can pass through. If the pump pulse induces perturbations in refractive index near the focus, a portion of the probe will be diffracted at an angle and collected by the imaging system with 7.5x magnification through the pickoff mirror. The spatial resolution of the dark-field imaging system is about 13 μm. The interaction region is also probed transversely with shadowgraphy by another 532nm, 10 ps laser pulse. During the experiment the vacuum laser intensity was in the range of $a_0 = 0.9 - 1.4$, and there was a weak prepulse 25 ns before the main laser pulse. While the prepulse may affect the channel formation, it is not our intention to study its effects in detail.

Longitudinal dark-field images and transverse shadowgrams from 4 laser shots are presented in Fig. 12. The probe delay for the shadowgraphy is fixed at approximately 50 − 100 ps after the pump pulse, which enters the plasma from the left of the shadowgrams. Figures 12(a) and 12(e) represent the case that the laser pulse breaks into multiple filaments, as evidenced by numerous low-intensity speckles on the dark-field beam profile (Fig. 12(a)) and multiple, short streaks on the shadowgram (Fig. 12(e)). Plasma channel formation is evi-

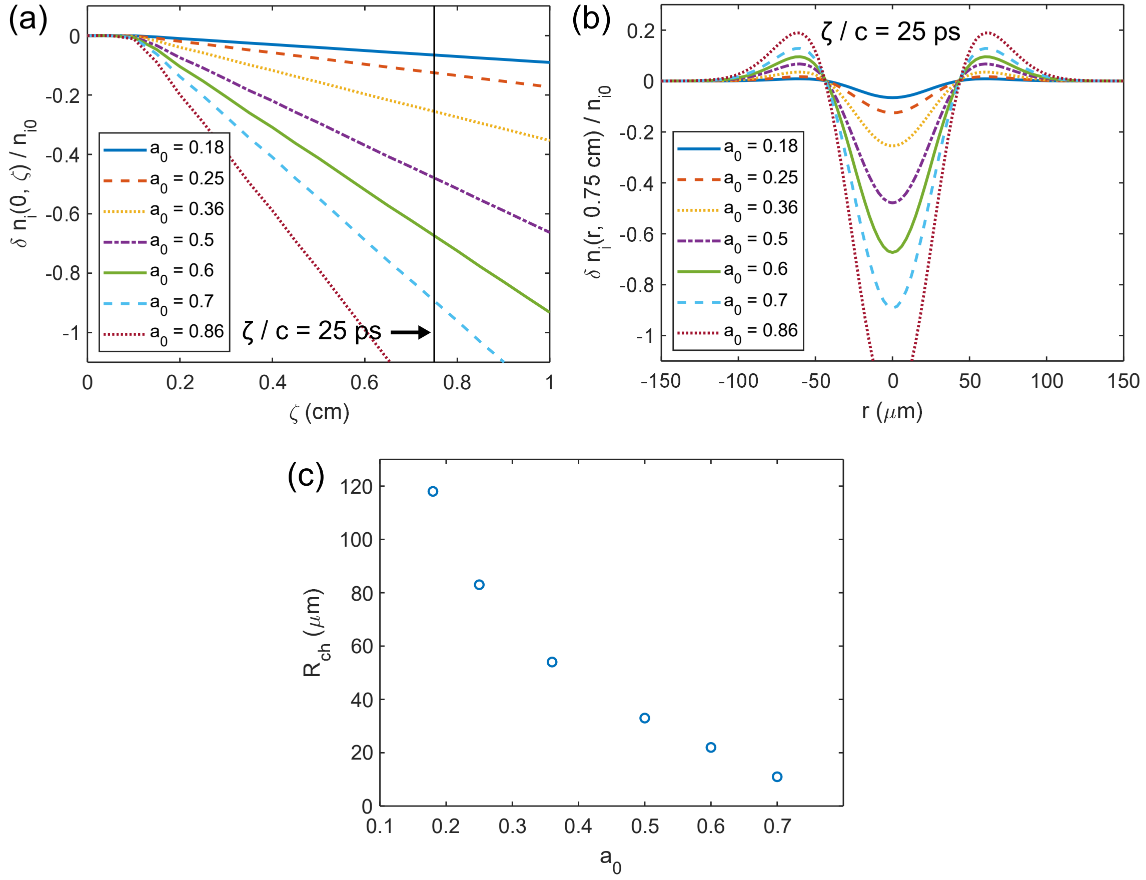

FIG. 7. (a) Temporal evolution of on-axis ion density perturbations up to $\zeta/c = 33$ ps, and (b) radial ion channel profiles at $\zeta/c = 25$ ps, calculated at $T_e = 0.2$ keV with a range of peak laser intensity $(0.4 - 9) \times 10^{15}$ W/cm^2, corresponding to $a_0 = 0.18$ – 0.86 in a hydrogen plasma. (c) Channel radii R_{ch} at $\zeta/c = 25$ ps with various a_0 are obtained from (b). The laser pulse duration is 3.5 ps.

dent in Figs. 12(b), (f) and Figs. 12(c), (g). In Fig. 12(b), a portion of the probe energy is coupled into a guiding structure with a small radius formed 40 ps after the pump pulse, and then exits the waveguide with a large divergence angle so that it is distinguished from the uncoupled portion of the probe and recorded by the dark-field imaging. The image reveals that the probe beam mode contains two spots separated by 21 μm, and the spot $1/e^2$ radius is 17 μm. The pump pulse in this case breaks into two spots, and each spot undergoes self-guiding and forms its own channel structure in the plasma. One of the ∼ 1-mm-long channels can be seen in Fig. 12(f), while the other one is not visible due to the probe geometry. The ∼ 1-mm-long plasma channel is also observed in Fig. 12(g). For this shot, the dark-field probe delay is moved to 573 ps, and the ring-shaped profile with 50 μm diameter shown in Fig. 12(c) indicates the remnant of the guiding channel at a much longer delay after the pump pulse than that in Fig 12(b). On the other hand, Figs. 12(d) and 12(h) show the effect of a strong prepulse: the blast wave forms cylindrical density shells, which is observed from the dark-field image (Fig. 12(d)) prior to the arrival of the main pump pulse. The structure is then recorded on the shadowgram (Fig. 12(e)) after the passage of the pump pulse. Note that in our dark-field imaging apparatus, some Fourier components at the object plane cannot be imaged, and therefore some portion of the ring profiles in Figs. 12(c) (corresponding to remnant of the plasma channel) and 12(d) (corresponding to prepulse-formed high-density shells) is missing. This can be mitigated by replacing the rectangular mirror in Fig. 11 by one with a central hole to collect the diffracted components axisymmetrically. This technique may be useful as a general diagnostic tool in experiments of intense laser-plasma interactions.

VI. CONCLUSION

In conclusion, we applied a technique of hydrodynamic shock compression and shaping of a mm-scale, near-atmospheric-pressure hydrogen gas, for proton acceleration near the critical density using a short-pulse CO$_2$ laser at ∼ 10 μm wavelength. The method is based on ablation of a solid in the vicinity of the gas jet nozzle by a nanosecond Nd:YAG laser with independent control of

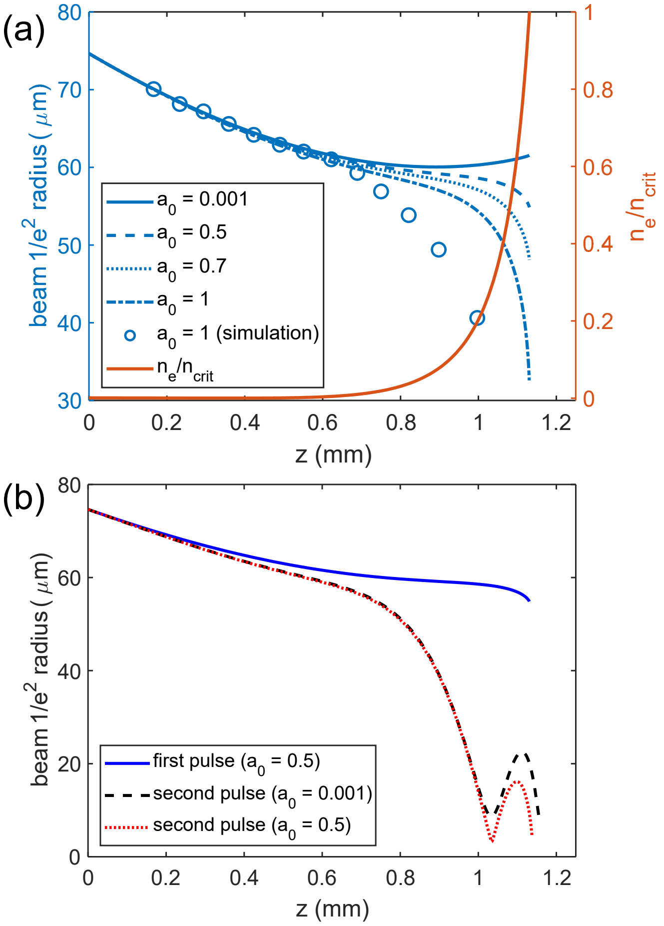

FIG. 8. Calculated laser beam radius evolution with SDE formalism for the cases of (a) propagation in the plasma density up-ramp without preformed structures, and (b) propagation of the first laser pulse with $a_0 = 0.5$ in the same density ramp, followed by a second laser pulse encountering an ion channel produced by the first pulse. The channel parameters $R_{\rm ch}$ and $\delta n_i/n_{i0}$ are acquired from Fig. 7.

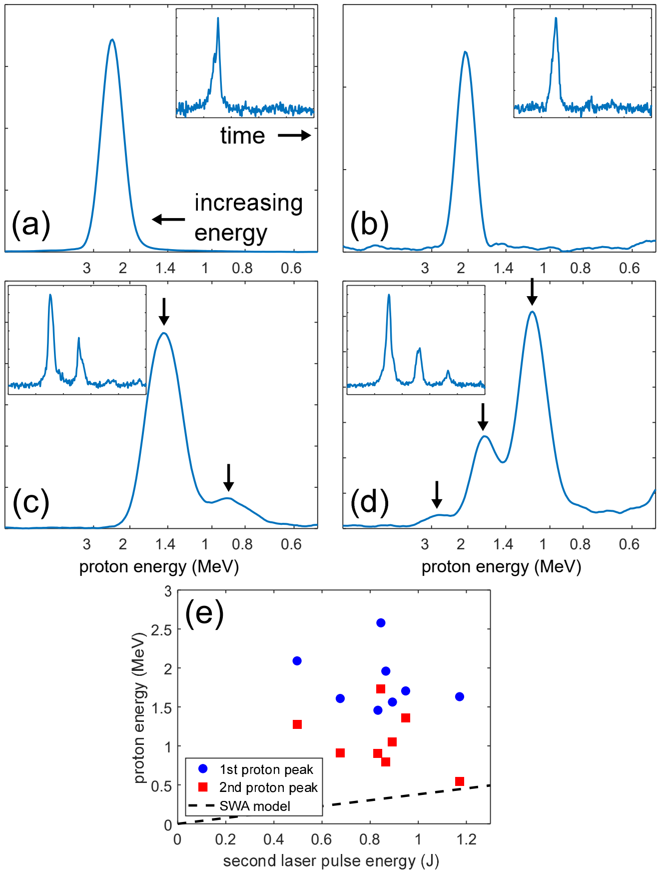

FIG. 9. Examples of Thomson parabola image lineouts from the "outlier" shots marked in Fig. 4, showing the features of (a)(b) single and (c)(d) multiple proton spectral peaks. Insets are the corresponding streak camera traces showing (a)(b) zero or negligible post pulses, and (c)(d) a significant post pulse after the main pulse. Arrows in (c) and (d) marks the location of the spectral peaks. The Thomson parabola lineouts here are not deconvolved with the size of the entrance pinhole. These outlier shots with laser post pulses and multiple proton spectra peaks are reproduced in (e) with the post pulse (second one in the pulse train) energy and two highest proton spectral peaks. The SWA model prediction is also shown in black dashed line in (e).

timing and energy. At a modest laser intensity of $a_0 \sim 1$, MeV quasi-monoenergetic protons can be routinely produced with an energy spread $\lesssim 10\%$, and a maximum energy of 2.5 MeV was recorded during the experiment. While shock wave acceleration is generally considered the origin of quasi-monoenergetic ions in this regime, through PIC simulations we identified a two-stage acceleration mechanism, which is first initiated in the underdense density up-ramp and then further accelerated by the electrostatic shock launched into the critical surface of the plasma.

As more experiments on near-critical, high-intensity laser-plasma interactions with gaseous targets are demonstrated during the recent years, shaping and steepening of plasma density profile, for preventing laser energy loss through nonlinear processes such as instabilities and filamentation in the underdense layer in front of the overdense region, has become increasingly important. However, we found that within the residual underdense layer left behind by the hydrodynamic shock front in the gas, nonlinear propagation effects may result to increased laser intensity delivered to the critical surface. These nonlinear effects include relativistic and ponderomotive self-focusing, and, for lasers with multi-pulse outputs, channel-focusing of the second pulse by a hollow ion channel created by the first pulse. Indirect evidence was noticed, including proton energies much higher than predictions by models and simulations, large shot-to-shot fluctuations of proton beam pointing angle, and multiple proton spectral peaks from the experimental results. In addition, ~ 2 MeV proton beams with a small divergence angle of ~ 8 mrad was recorded. The origin of collimated energetic protons is not understood and requires further investigations.

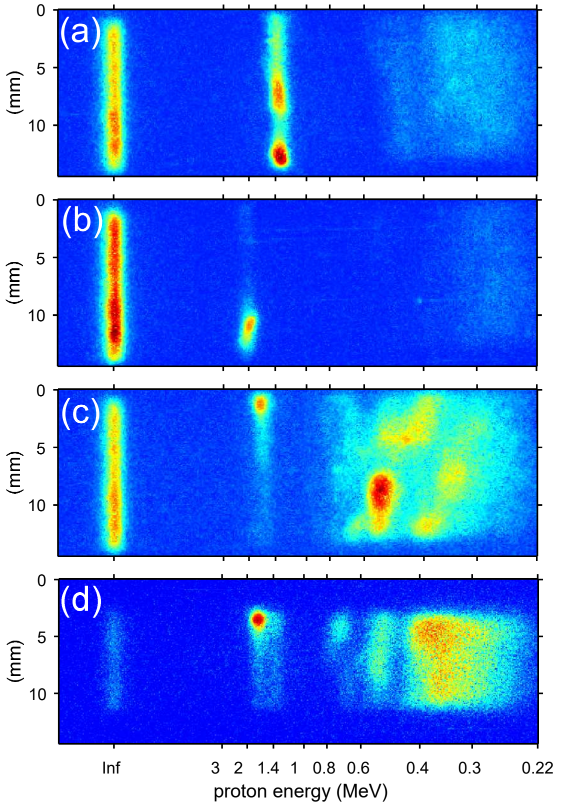

FIG. 10. Selected space-resolved proton spectra showing 1-D collimated spectral components between $\sim 1.2 - 2$ MeV, with narrow energy spreads and erratic pointing angles, as well as low energy ($\lesssim 0.5$ MeV), relatively uniform components. "Inf" on energy axis represents direct line of sight from the interaction point, which is ~ 30 cm before the scintillator.

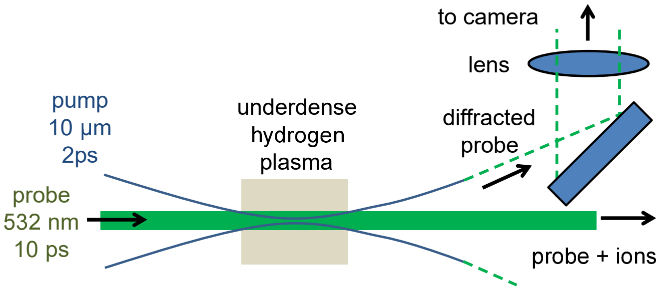

FIG. 11. Experimental setup of dark-field imaging for probing the hollow plasma channel produced by the intense CO_2 laser pulse at ~ 10 μm wavelength.

Analyses showed that an ion channel can be formed in the hydrogen plasma with similar parameters used in our experiment. Quasi-static laser beam size evolution calculated from SDE method showed that both self-focusing and channel-focusing are capable of significantly reducing the laser beam size while propagating in the shock-tailored plasma density ramp used in the experiment. While formation of ion channels has been reported in previous works, we did not attempt to directly observe them in our proton acceleration experiment. This was performed in a subsequent channel observing experiment where a longitudinal dark-field imaging diagnostic was employed with a 10-ps, 532 nm probe pulse collinear with the pump CO_2 laser pulse. Coupling and guiding a small portion of the probe pulse through the pump-produced ion channel was observed, together with $\sim$ mm-long channels recorded by a transverse shadowgraphy diagnostic, for picosecond CO_2 laser pulses with $a_0 \sim 1$ in the hydrogen plasma.

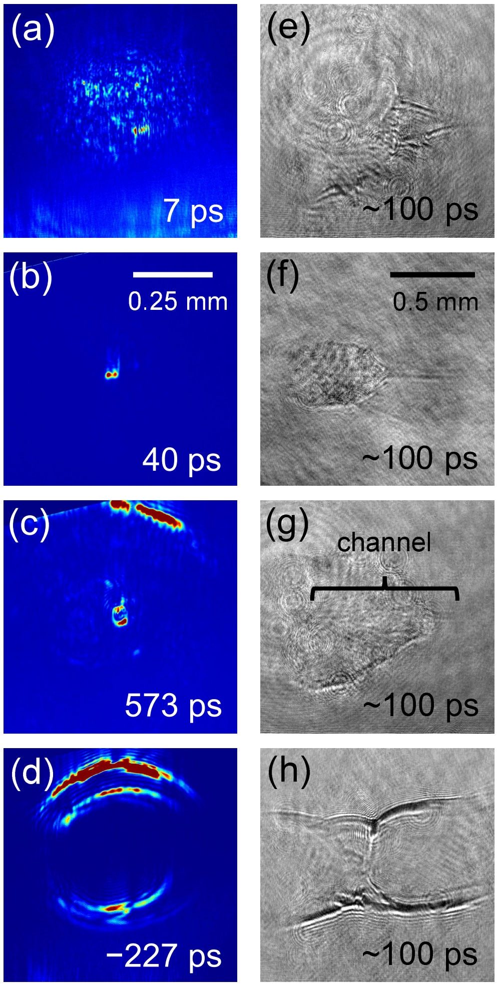

FIG. 12. Longitudinal dark-field images at (a) 7 ps, (b) 40 ps, (c) 573 ps, and (d) −227 ps, and (e)(f)(g)(h) their corresponding transverse shadowgrams at a fixed delay of ~ 100 ps. The pump laser enters the plasma from the left of the shadowgrams. For (e)–(g), the partial oval structure is caused by the low-energy 25 ns prepulse.

ACKNOWLEDGMENTS

The authors thank D. Kaganovich, A. Davidson, and N. Cook for useful discussions. The authors also thank C.-H. Pai for sharing the ATF laser beam time. This work is supported by U.S. Department of Energy and

NRL base programs.

[1] S. P. Hatchett, C. G. Brown, T. E. Cowan, E. A. Henry, J. S. Johnson, M. H. Key, J. A. Koch, A. B. Langdon, B. F. Lasinski, R. W. Lee, A. J. Mackinnon, D. M. Pennington, M. D. Perry, T. W. Phillips, M. Roth, T. C. Sangster, M. S. Singh, R. A. Snavely, M. A. Stoyer, S. C. Wilks, and K. Yasuike, “Electron, photon, and ion beams from the relativistic interaction of petawatt laser pulses with solid targets,” Physics of Plasmas **7**, 2076–2082 (2000).

[2] S. C. Wilks, A. B. Langdon, T. E. Cowan, M. Roth, M. Singh, S. Hatchett, M. H. Key, D. Pennington, A. MacKinnon, and R. A. Snavely, “Energetic proton generation in ultra-intense laser–solid interactions,” Physics of Plasmas **8**, 542–549 (2001).

[3] T. Esirkepov, M. Borghesi, S. V. Bulanov, G. Mourou, and T. Tajima, “Highly efficient relativistic-ion generation in the laser-piston regime,” Phys. Rev. Lett. **92**, 175003 (2004).

[4] O. Klimo, J. Psikal, J. Limpouch, and V. T. Tikhonchuk, “Monoenergetic ion beams from ultrathin foils irradiated by ultrahigh-contrast circularly polarized laser pulses,” Phys. Rev. ST Accel. Beams **11**, 031301 (2008).

[5] A. Henig, S. Steinke, M. Schnürer, T. Sokollik, R. Hörlein, D. Kiefer, D. Jung, J. Schreiber, B. M. Hegelich, X. Q. Yan, J. Meyer-ter Vehn, T. Tajima, P. V. Nickles, W. Sandner, and D. Habs, “Radiation-pressure acceleration of ion beams driven by circularly polarized laser pulses,” Phys. Rev. Lett. **103**, 245003 (2009).

[6] L. Yin, B. J. Albright, B. M. Hegelich, and J. C. Fernández, “Gev laser ion acceleration from ultrathin targets: The laser break-out afterburner,” Laser and Particle Beams **24**, 291–298 (2006).

[7] A. Henig, D. Kiefer, K. Markey, D. C. Gautier, K. A. Flippo, S. Letzring, R. P. Johnson, T. Shimada, L. Yin, B. J. Albright, K. J. Bowers, J. C. Fernández, S. G. Rykovanov, H.-C. Wu, M. Zepf, D. Jung, V. K. Liechtenstein, J. Schreiber, D. Habs, and B. M. Hegelich, “Enhanced laser-driven ion acceleration in the relativistic transparency regime,” Phys. Rev. Lett. **103**, 045002 (2009).

[8] T. Nakamura, S. V. Bulanov, T. Z. Esirkepov, and M. Kando, “High-energy ions from near-critical density plasmas via magnetic vortex acceleration,” Phys. Rev. Lett. **105**, 135002 (2010).

[9] S. S. Bulanov, V. Y. Bychenkov, V. Chvykov, G. Kalinchenko, D. W. Litzenberg, T. Matsuoka, A. G. R. Thomas, L. Willingale, V. Yanovsky, K. Krushelnick, and A. Maksimchuk, “Generation of gev protons from 1 pw laser interaction with near critical density targets,” Physics of Plasmas **17**, 043105 (2010).

[10] C. A. J. Palmer, N. P. Dover, I. Pogorelsky, M. Babzien, G. I. Dudnikova, M. Ispiriyan, M. N. Polyanskiy, J. Schreiber, P. Shkolnikov, V. Yakimenko, and Z. Najmudin, “Monoenergetic proton beams accelerated by a radiation pressure driven shock,” Phys. Rev. Lett. **106**, 014801 (2011).

[11] D. Haberberger, S. Tochitsky, F. Fiuza, C. Gong, R. A. Fonseca, L. O. Silva, W. B. Mori, and C. Joshi, “Collisionless shocks in laser-produced plasma generate monoenergetic high-energy proton beams,” Nature Physics **8**, 95–99 (2012).

[12] S. Palaniyappan, C. Huang, D. C. Gautier, C. E. Hamilton, M. A. Santiago, C. Kreuzer, A. B. Sefkow, R. C. Shah, and J. C. Fernández, “Efficient quasi-monoenergetic ion beams from laser-driven relativistic plasmas,” Nature Communications **6**, 10170 (2015).

[13] O. Tresca, N. P. Dover, N. Cook, C. Maharjan, M. N. Polyanskiy, Z. Najmudin, P. Shkolnikov, and I. Pogorelsky, “Spectral modification of shock accelerated ions using a hydrodynamically shaped gas target,” Phys. Rev. Lett. **115**, 094802 (2015).

[14] I. V. Pogorelsky, M. Babzien, I. Ben-Zvi, M. N. Polyanskiy, J. Skaritka, O. Tresca, N. P. Dover, Z. Najmudin, W. Lu, N. Cook, A. Ting, and Y.-H. Chen, “Extending laser plasma accelerators into the mid-IR spectral domain with a next-generation ultra-fast CO2 laser,” Plasma Physics and Controlled Fusion **58**, 034003 (2016).

[15] S. C. Wilks, W. L. Kruer, M. Tabak, and A. B. Langdon, “Absorption of ultra-intense laser pulses,” Phys. Rev. Lett. **69**, 1383–1386 (1992).

[16] A. Macchi, F. Cattani, T. V. Liseykina, and F. Cornolti, “Laser acceleration of ion bunches at the front surface of overdense plasmas,” Phys. Rev. Lett. **94**, 165003 (2005).

[17] F. Fiuza, R. A. Fonseca, J. Tonge, W. B. Mori, and L. O. Silva, “Weibel-instability-mediated collisionless shocks in the laboratory with ultraintense lasers,” Physical Review Letter **108**, 235004 (2012).

[18] F. Fiuza, A. Stockem, E. Boella, R. A. Fonseca, L. O. Silva, D. Haberberger, S. Tochitsky, C. Gong, W. B. Mori, and C. Joshi, “Laser-driven shock acceleration of monoenergetic ion beams,” Phys. Rev. Lett. **109**, 215001 (2012).

[19] S. N. Chen, M. Vranic, T. Gangolf, E. Boella, P. Antici, M. Bailly-Grandvaux, P. Loiseau, H. Pépin, G. Revet, J. J. Santos, A. M. Schroer, M. Starodubtsev, O. Willi, L. O. Silva, E. d’Humières, and J. Fuchs, “Collimated protons accelerated from an overdense gas jet irradiated by a 1 µm wavelength high-intensity short-pulse laser,” Scientific Reports **7**, 13505 (2017).

[20] P. Puyuelo-Valdes, J. L. Henares, F. Hannachi, T. Ceccotti, J. Domange, M. Ehret, E. d’Humieres, L. Lancia, J.-R. Marquès, X. Ribeyre, J. J. Santos, V. Tikhonchuk, and M. Tarisien, “Proton acceleration by collisionless shocks using a supersonic h2 gas-jet target and high-power infrared laser pulses,” Physics of Plasmas **26**, 123109 (2019).

[21] W. L. Kruer, *The Physics of Laser Plasma Interactions* (2003).

[22] P. McKenna, D. C. Carroll, O. Lundh, F. Nürnberg, K. Markey, S. Bandyopadhyay, D. Batani, R. G. Evans, R. Jafer, S. Kar, D. Pepler, M. N. Quinn, R. Redaelli, M. Roth, C.-G. Wahlström, X. H. Yuan, and M. Zepf, “Effects of front surface plasma expansion on proton acceleration in ultraintense laser irradiation of foil targets,” Laser and Particle Beams **26**, 591–596 (2008).

[23] D. B. Zou, H. B. Zhuo, X. H. Yang, F. Q. Shao, Y. Y. Ma, T. P. Yu, H. C. Wu, Y. Yin, Z. Y. Ge, and X. H. Li, “Enhanced target normal sheath acceleration based on the laser relativistic self-focusing,” Physics of Plasmas **21**, 063103 (2014).

[24] Y. Sentoku, V. Y. Bychenkov, K. Flippo, A. Maksimchuk, K. Mima, G. Mourou, Z. M. Sheng, and D. Umstadter, “High-energy ion generation in interaction. of short laser pulse with high-density plasma,” Applied Physics B **74**, 207–215 (2002).

[25] L. A. Gizzi, E. Boella, L. Labate, F. Baffigi, P. J. Bilbao, F. Brandi, G. Cristoforetti, A. Fazzi, L. Fulgentini, D. Giove, P. Koester, D. Palla, and P. Tomassini, “Enhanced laser-driven proton acceleration via improved fast electron heating in a controlled pre-plasma,” Scientific Reports **11**, 13728 (2021).

[26] T. P. Frazer, R. Wilson, M. King, N. M. H. Butler, D. C. Carroll, M. J. Duff, A. Higginson, J. Jarrett, Z. E. Davidson, C. Armstrong, H. Liu, D. Neely, R. J. Gray, and P. McKenna, “Enhanced laser intensity and ion acceleration due to self-focusing in relativistically transparent ultrathin targets,” Phys. Rev. Research **2**, 042015 (2020).

[27] K. Krushelnick, A. Ting, C. I. Moore, H. R. Burris, E. Esarey, P. Sprangle, and M. Baine, “Plasma channel formation and guiding during high intensity short pulse laser plasma experiments,” Phys. Rev. Lett. **78**, 4047–4050 (1997).

[28] E. Esarey, P. Sprangle, J. Krall, and A. Ting, “Self-focusing and guiding of short laser pulses in ionizing gases and plasmas,” IEEE Journal of Quantum Electronics **33**, 1879–1914 (1997).

[29] M. N. Polyanskiy, M. Babzien, and I. V. Pogorelsky, “Chirped-pulse amplification in a co2 laser,” Optica **2**, 675–681 (2015).

[30] D. Kaganovich, M. H. Helle, D. F. Gordon, and A. Ting, “Measurements and simulations of shock wave generated plasma-vacuum interface,” Physics of Plasmas **18**, 120701 (2011).

[31] D. Kaganovich, D. F. Gordon, M. H. Helle, and A. Ting, “Shaping gas jet plasma density profile by laser generated shock waves,” Journal of Applied Physics **116**, 013304 (2014).

[32] M. H. Helle, D. F. Gordon, D. Kaganovich, Y. Chen, J. P. Palastro, and A. Ting, “Laser-accelerated ions from a shock-compressed gas foil,” Phys. Rev. Lett. **117**, 165001 (2016).

[33] L. I. Sedov, *Similarity and Dimensional Methods in Mechanics*,

4th ed. (Academic Press, 1959).

[34] I. B. Zeldovich and I. P. Raizer, *Physics of Shock Waves and High-Temperature Hydrodynamic Phenomena* (Dover, 2002).

[35] Y. Liu, I. Pogorelsky, and D. Cline, "Gas breakdown limit and maximum acceleration gradient for inverse cherenkov laser accelerator," Nuclear Instruments and Methods in Physics Research Section A: Accelerators, Spectrometers, Detectors and Associated Equipment **430**, 171–179 (1999).

[36] J. N. Olsen, G. W. Kuswa, and E. D. Jones, "Ion-expansion energy spectra correlated to laser plasma parameters," Journal of Applied Physics **44**, 2275–2283 (1973).

[37] J. F. Ziegler, M. Ziegler, and J. Biersack, "SRIM – the stopping and range of ions in matter (2010)," Nuclear Instruments and Methods in Physics Research Section B: Beam Interactions with Materials and Atoms **268**, 1818–1823 (2010), 19th International Conference on Ion Beam Analysis.

[38] N. Cook, O. Tresca, and R. Lefferts, "Scintillator diagnostics for the detection of laser accelerated ion beams," Journal of Instrumentation **9**, P09004–P09004 (2014).

[39] D. Gordon, W. Mori, and T. Antonsen, "A ponderomotive guiding center particle-in-cell code for efficient modeling of laser-plasma interactions," IEEE Transactions on Plasma Science **28**, 1135–1143 (2000).

[40] D. F. Gordon, "Improved ponderomotive guiding center algorithm," IEEE Transactions on Plasma Science **35**, 1486–1488 (2007).

[41] D. F. Gordon, "turboWAVE simulation framework," `https://doi.org/10.5281/zenodo.6402222` (2022).

[42] S. Glowacz, H. Hora, J. Badziak, S. Jablonski, Y. Cang, and F. Osman, "Analytical description of rippling effect and ion acceleration in plasma produced by a short laser pulse," Laser and Particle Beams **24**, 15–25 (2006).

[43] B. Hafizi, A. Ting, R. F. Hubbard, P. Sprangle, and J. R. Peñano, "Relativistic effects on intense laser beam propagation in plasma channels," Physics of Plasmas **10**, 1483–1492 (2003).

[44] P. Sprangle, A. Ting, and C. M. Tang, "Radiation focusing and guiding with application to the free electron laser," Phys. Rev. Lett. **59**, 202–205 (1987).

[45] P. Sprangle, A. Ting, and C. M. Tang, "Analysis of radiation focusing and steering in the free-electron laser by use of a source-dependent expansion technique," Phys. Rev. A **36**, 2773–2781 (1987).

[46] T. Tajima and J. M. Dawson, "Laser electron accelerator," Phys. Rev. Lett. **43**, 267–270 (1979).

[47] R. F. Hubbard, B. Hafizi, A. Ting, D. Kaganovich, P. Sprangle, and A. Zigler, "High intensity focusing of laser pulses using a short plasma channel lens," Physics of Plasmas **9**, 1431–1442 (2002).

[48] After correcting misprints (sign errors) in Eq. 7(b) (which also leads to corrections in Eq. 8(b)) in Ref. 43.

[49] S.-Y. Chen, G. S. Sarkisov, A. Maksimchuk, R. Wagner, and D. Umstadter, "Evolution of a plasma waveguide created during relativistic-ponderomotive self-channeling of an intense laser pulse," Phys. Rev. Lett. **80**, 2610–2613 (1998).

[50] L. Willingale, P. M. Nilson, A. G. R. Thomas, J. Cobble, R. S. Craxton, A. Maksimchuk, P. A. Norreys, T. C. Sangster, R. H. H. Scott, C. Stoeckl, C. Zulick, and K. Krushelnick, "High-power, kilojoule class laser channeling in millimeter-scale underdense plasma," Phys. Rev. Lett. **106**, 105002 (2011).

[51] L. Willingale, A. G. R. Thomas, P. M. Nilson, H. Chen, J. Cobble, R. S. Craxton, A. Maksimchuk, P. A. Norreys, T. C. Sangster, R. H. H. Scott, C. Stoeckl, C. Zulick, and K. Krushelnick, "Surface waves and electron acceleration from high-power, kilojoule-class laser interactions with underdense plasma," New Journal of Physics **15**, 025023 (2013).

[52] P. Sprangle, J. Krall, and E. Esarey, "Hose-modulation instability of laser pulses in plasmas," Phys. Rev. Lett. **73**, 3544–3547 (1994).

[53] N. M. Naumova, J. Koga, K. Nakajima, T. Tajima, T. Z. Esirkepov, S. V. Bulanov, and F. Pegoraro, "Polarization, hosing and long time evolution of relativistic laser pulses," Physics of Plasmas **8**, 4149–4155 (2001).

[54] C. Ren and W. B. Mori, "Physical picture for the laser hosing instability in a plasma," Physics of Plasmas **8**, 3118–3119 (2001).

[55] G. Li, R. Yan, C. Ren, T.-L. Wang, J. Tonge, and W. B. Mori, "Laser channeling in millimeter-scale underdense plasmas of fast-ignition targets," Phys. Rev. Lett. **100**, 125002 (2008).

[56] M. N. Polyanskiy, I. V. Pogorelsky, M. Babzien, and M. A. Palmer, "Demonstration of a 2 ps, 5 tw peak power, long-wave infrared laser based on chirped-pulse amplification with mixed-isotope co2 amplifiers," OSA Continuum **3**, 459–472 (2020).